Fast high-resolution 3D total internal reflection fluorescence microscopy by incidence angle scanning and azimuthal averaging

Jérôme Boulanger[a,1], Charles Gueudry[b,c], Daniel Münch[b,c], Bertrand Cinquin[a], Perrine Paul-Gilloteaux[a,b], Sabine Bardin[a], Christophe Guérin[d], Fabrice Senger[d], Laurent Blanchoin[d], and Jean Salamero[a,b,1]

[a]UMR144 CNRS/Institut Curie, 75005 Paris, France; [b]Plateforme Imagerie Cellulaire et Tissulaire–Infrastructure en Biologie Santé et Agronomie Institut Curie, 75005 Paris, France; [c]Roper Scientific SAS, 91017 Evry, France; and [d]Institut de Recherches en Technologies et Sciences pour le Vivant, Laboratoire de Physiologie Cellulaire et Végétale, CNRS/Commissariat à l'Energie Atomique/Institut National de la Recherche Agronomique/Université Joseph Fourier, Grenoble 38054, France

Edited by Jennifer Lippincott-Schwartz, National Institutes of Health, Bethesda, MD, and approved October 7, 2014 (received for review August 18, 2014)

Total internal reflection fluorescence microscopy (TIRFM) is the method of choice to visualize a variety of cellular processes in particular events localized near the plasma membrane of live adherent cells. This imaging technique not relying on particular fluorescent probes provides a high sectioning capability. It is, however, restricted to a single plane. We present here a method based on a versatile design enabling fast multiwavelength azimuthal averaging and incidence angles scanning to computationally reconstruct 3D images sequences. We achieve unprecedented 50-nm axial resolution over a range of 800 nm above the coverslip. We apply this imaging modality to obtain structural and dynamical information about 3D actin architectures. We also temporally decipher distinct Rab11a-dependent exocytosis events in 3D at a rate of seven stacks per second.

TIRFM | high resolution | living cells | 3D image reconstruction | membrane recycling

High-resolution techniques relying on specific fluorescent probes (1–5) allow imaging at the nanometer scale. However, they impose severe constraints on tagging and cannot be easily combined with colocalization (6) (photoactivated localization microscopy or stochastic optical reconstruction microscopy). In general, these approaches improve resolution at the expense of a low image acquisition rate. Structured illumination microscopy (SIM), although not relying on particular properties of fluorescent probes such as photoconversion and being well suited for multicolor tagging (7, 8), still requires the acquisition of a number of raw images (ranging from 9 to 15 images) to build a single full doubled resolved optical section. Consequently, despite recent advances (9), SIM remains poorly adapted to fast imaging of dynamical events. Finally, with the noticeable exception of sophisticated combinations (4), most of these methods use illumination configurations that expose the entire sample thickness to intense light radiation. Therefore, phototoxic effect of whole-cell illumination is often a limitation for live cell imaging.

In total internal reflection fluorescence microscopy (TIRFM), fluorophores are excited with evanescent waves that intensity decays exponentially with the distance from the interface (10). The imaged section is therefore thinner (100–200 nm) in comparison with most optical sectioning techniques like confocal (11) or multiphoton microscopy (12), whose temporal resolutions are additionally limited. Therefore, TIRFM is particularly suitable for imaging the plasma membrane where fundamental cellular mechanisms related to cell/substrate contact regions, secretory and endocytic processes (13), binding of ligands to cell surface receptors, and dynamical remodeling of cytoskeleton elements take place. High temporal resolution is required as, for example, docking of vesicles to the plasma membrane may last for less than half a second (14) and fusion events can be complete in less than 300 ms (15). If classical TIRFM exhibits modulation patterns that prevent accurate quantification analysis, elimination of these artifacts can be achieved by varying the azimuthal angle of the illumination beam during the exposure time (16, 17) and an accurate control of the incident beam orientation (18). Finally, multiple incidence angle TIRFM measurements can be further exploited to map the cell membrane (19, 20), the depth of vesicles (21), or microtubules filaments (22) using the relationship between the illumination angle and the penetration depth of the evanescent wave, thus adding a third dimension to TIRFM imaging. However, to our knowledge, these approaches remain in the realm of localization techniques, whereas reconstruction of high-resolution 3D volume from multiangle total internal reflection fluorescence (TIRF) image stacks has not yet been reported.

We present a TIRF-based approach enabling the acquisition multiangle stacks of images in time lapse combined with a method to estimate the tridimensional density of fluorophores. The reconstruction of multiangle stacks is based on the inversion of a theoretical model of the imaging operator. We have validated this model on calibrated samples and challenged the proposed reconstruction approach on actin cytoskeleton organization in vitro or near the cell surface of living cells. We also demonstrate the time and axial resolving capability of our approach with the study of intracellular markers involved in fast vesicle trafficking from the cell depth down to fusion sites at the plasma membrane.

Significance

Recent progress has pushed forward the resolving capacity of optical microscopy at the expense of a low acquisition rate and use of specific probes. Such limitations make these techniques incompatible with dynamics localization of multiple elements in single cell. We report here a method to recover 3D volumes from images obtained using several total internal reflection fluorescence (TIRF) incidence angles at dense regime of acquisition. This approach allows investigating several dynamical processes occurring in depth of the cell up to 800 nm from the plasma membrane such as actin remodeling. The study of time-correlated molecular behaviors at the very late steps of vesicle docking–fusion during exocytosis of two distinct recycling transport intermediates, in 3D and at high axial resolution, is also accessible.

Author contributions: J.B., C. Gueudry, D.M., and J.S. designed research; J.B., C. Gueudry, D.M., B.C., S.B., C. Guérin, F.S., L.B., and J.S. performed research; S.B., C. Guérin, F.S., and L.B. contributed new reagents/analytic tools; J.B. and P.P.-G. analyzed data; and J.B., C. Gueudry, and J.S. wrote the paper.

Conflict of interest statement: C. Gueudry and D.M. were employees for Roper Scientific at the time of the writing of the article.

This article is a PNAS Direct Submission.

[1]To whom correspondence may be addressed. Email: jerome.boulanger@curie.fr or salamero@curie.fr.

This article contains supporting information online at www.pnas.org/lookup/suppl/doi:10.1073/pnas.1414106111/-/DCSupplemental.

Results

Multiangle Azimuthal Averaging TIRFM. In objective-based TIRFM, an evanescent wave is created at the output of the objective by a laser beam focused in the back focal plane (BFP) of the objective. As depicted in Fig. S1*A*, the output incidence angle θ of the beam is determined in the BFP by the radial distance r between the focused beam and the optical axis such that $r = n_i f \sin\theta$, where n_i is the optical index of the glass and f is the focal length of the objective. To scramble ring and fringe interference patterns induced by dusts and filters and obtain an even illumination, we use galvanometers (17). The beam spins circularly during the exposure time, so that each point of the described circle corresponds to the same incidence angle θ, but not the same azimuthal angle φ. To assess the quality of the proposed setup, we have imaged the BFP of the objective and recorded the trajectory of the focused beam for one and multiple azimuthal revolutions by varying the exposure time (Fig. S1*C*). In real image acquisition conditions, hardware synchronization maintains an integer number of circles during the exposure time, therefore ensuring a constant illumination across time. Kymographs (Fig. S1*D*) and profiles (Fig. S1*E*) show that the width of the circles remains stable for various incidence angles. Moreover, a measurement of the intensity at the BFP of the objective (Fig. S1*F*) shows that it does not depend on the azimuthal angle. Finally, the proposed approach allows using the fact that the penetration depth remains constant while interference patterns, which depend on φ, are averaged out and vanish. This is illustrated in Fig. 1 *A* and *B* where fluorescently labeled clathrin-coated plaques are illuminated with either a fixed or spinning azimuthal angle. Depending on the fluorescence distribution, even when not visible, modulations may alter the measurements and hinder quantitative analysis of the images (Fig. 2 *A* and *B*; zoomed area in right parts). The proposed approach achieves one revolution in 6.5 ms with optimal circle quality, enabling imaging of fast dynamics without compromise on the field of view. In the next experiments, the temporal resolution will not be limited by the scanning module but rather by the number of collected photons, phototoxicity, and the frame rate of the camera.

Using a dedicated component embedded in the acquisition software and the proposed high-speed motorization (*SI Materials and Methods* and Fig. S2 *A* and *B*), both the radial distance r and the excitation wavelength could be modified within less than 1 ms, allowing to adapt the penetration depth to the excitation wavelength or to create advanced acquisition protocols while using simultaneously exposure and readout ("streaming overlap" mode). As illustrated in the right part of Fig. S1*B*, classical TIRF acquisition where azimuthal and incidence angles are fixed (*Top Left*) or azimuthal spinning acquisition with fixed incidence angle (*Bottom Left*) are accessible. For more complex cases, such as time-lapse acquisition using sequentially total internal reflection (outer circle) and oblique wide-field (WF) (inner circle), illumination can be performed as shown in the top right scheme of Fig. S1*B*. Finally, a TIRF acquisition protocol where the penetration depth is adapted for two different wavelengths is illustrated by the last scheme (Fig. 1*B*, *Bottom Right*). In this case, the two channels can be detected simultaneously using a multichannel device while scanning the two colored circles one after the other within the same exposure time. Note that one of the circles may correspond to an incidence angle below the critical angle and leads to simultaneous WF and TIRF imaging of two distinct molecular entities.

To illustrate these capabilities, we have imaged M10 cells onto fibronectin-coated micropatterns and stably expressing Langerin genetically fused with eYFP in its luminal domain a transmembrane protein known to undergo constitutive recycling to the plasma membrane (23), using sequentially oblique WF (Fig. 1*C*, *Left*) and TIRF illumination (Fig. 1*C*, *Middle*). Emission yield of eYFP being strongly reduced by the pH environment of the endosomal-recycling compartments (15),

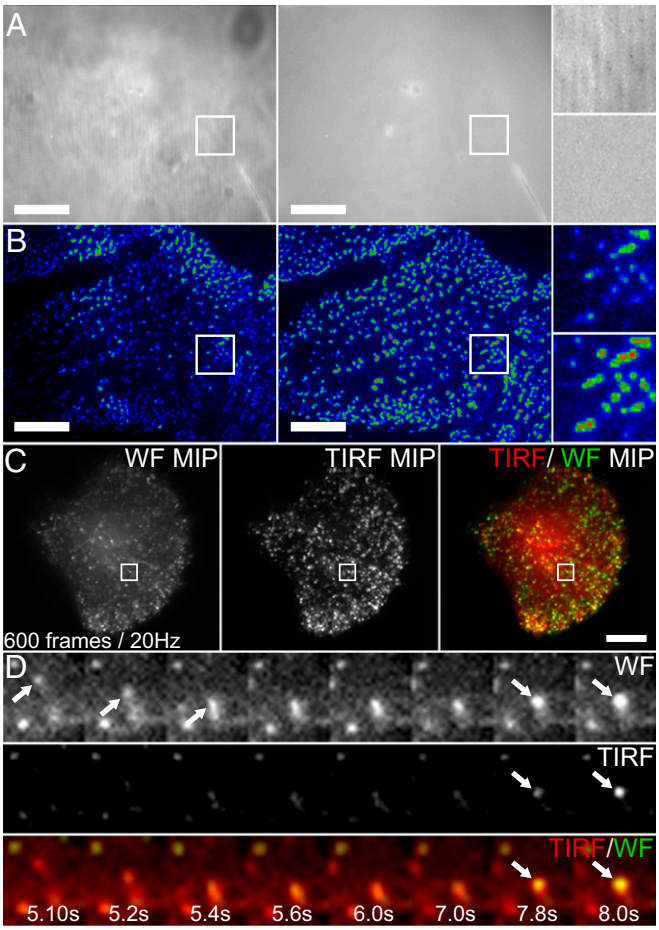

Fig. 1. TIRF artifact reductions by azimuthal averaging. (*A*) Thin fluorescent layer imaged using either fixed or spinning azimuth (same incidence angle). (*B*) Clathrin-coated plaques (AP2-mCherry in HeLa cells) acquired in both conditions. (Scale bars: 10 μm.) (*C*) Temporal maximum intensity projections of 600 image sequences of live M10 cells stably expressing eYFP-Langerin, acquired using sequential WF and TIRF illumination with an exposure time of 50 ms at 20 fps are displayed respectively on the *Left* and *Middle* pictures. On the *Right*, the WF (in green) and TIRF (in red) projections are overlaid. (Scale bar: 8 μm.) (*D*) Thumbnails display a time series at the zoomed position selected by white rectangle in *C* and illustrates the trajectory of a Langerin exocytic vesicle from inside the cell (WF, upper row) up to its docking and fusion event (TIRF, middle row) at the plasma membrane. An overlay of the WF (in green) and TIRF (in red) temporally defined fluorescent signals are finally shown in the last row.

a sudden increase of signal is an indicator of vesicle fusion at the cell surface. The overall dynamic process, which includes vesicle docking and fusion mechanisms, takes place within 2 s in a confined space, at first near and latter at the plasma membrane (Fig. 1*D*). By coupling azimuthal averaging with the sequential acquisition of images corresponding to two distinct incidence angles θ located on either side of the TIRF critical angle, behavior of vesicles from in depth the cell to the surface could be recorded with a frame rate of 20 frames per second (fps) over sequences lasting for up to few minutes providing a rough estimate of the depth localization over time of these vesicles (Movie S1). To further gain axial resolution, we considered multiangle TIRFM image stack acquisitions by increasing the number of incidence angles and investigated the 3D reconstruction of the resulting image stacks.

Three-Dimensional Reconstruction of Multiangle TIRFM Image Stacks. Images denoted $g(\theta)$ measured at each incidence angle θ result from the averaging of the intensity contribution obtained by

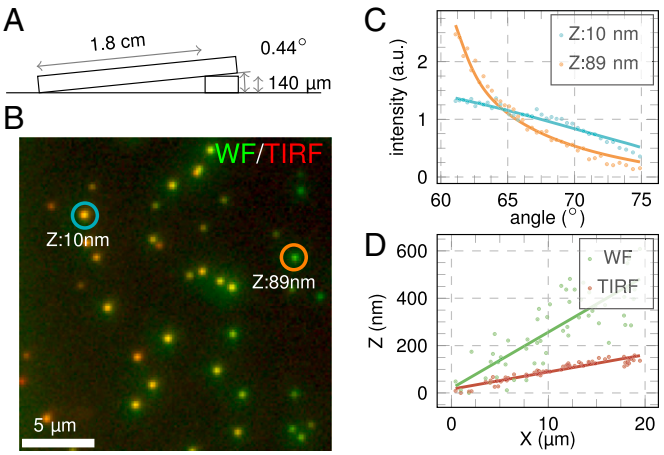

Fig. 2. Experimental validation of the multiangle TIRF model. (*A*) Schema of the system designed to create a slope of fluorescent beads. (*B*) Overlay of the maximum intensity projection of image stack acquired with WF and TIRF illumination. (Scale bar: 5 µm.) The evolution of the intensity versus the illumination angle θ of two selected beads are plotted in *C* with the corresponding fitting theoretical model (continuous line) for their estimated depth (respectively 10 and 89 nm). (*D*) Depth of all of the beads estimated by fitting the theoretical TIRF model (in red) and the depth of the same beads estimated by fitting a Gaussian model in the WF image stack (in green).

varying the azimuth φ during the exposure time and can be modeled by the following expression:

$$g(\theta) = \int_0^{2\pi} \int_0^{\infty} \int_{-\infty}^{\infty} I(z,\alpha,\varphi)\rho\left(\frac{\theta-\alpha}{\Omega/\cos\theta}\right) f(z)\, d\alpha dz d\varphi,$$

where $f(z)$ is the density of fluorophores in the medium convolved by the emission point spread function and $\rho(\cdot)$ represents the laser beam profile of divergence Ω. The function $I(z,\alpha,\varphi)$ describes the intensity of the electric field as a function of the depth z, the incidence angle α, and the azimuth φ. For an incidence angle α greater than the critical angle, an exponentially decreasing component appears whose characteristic penetration depth $d(\alpha)$ can be expressed as a function of the wavelength λ, the refractive index of the glass n_i, and the refractive index of the medium n_t as $d(\alpha) = \lambda/4\pi\,(n_i^2 \sin^2\alpha + n_t^2)^{-1/2}$. A more realistic model would take into account a multilayer dielectric material (24). However, for small enough depth ($z < \lambda/2$), the TIRF excitation intensity can be approximated by a simple exponentially decaying function (25). For a given angle θ, we can average the contributions of the two polarization components when the beam describes a full circle. Finally, by considering a finite set of incident angles θ and depth z, we can discretize the problem and obtain the following linear system of equations $\boldsymbol{g} = \boldsymbol{H}\boldsymbol{f}$, where $\boldsymbol{H}$ is the matrix associated to the operator involved in the image formation (Fig. S3*B*).

To validate the proposed model, a test sample has been designed containing fluorescent beads located at different heights as previously described (17). A multiangle TIRF and a WF image stacks of the sample have been acquired (Fig. 2*B*), and a parametric model of the beads viewed through the image formation operator (*SI Imaging Model and Reconstruction*) has been fitted to the evolution of the intensity versus the incident TIRF angle (21). It is worth stressing that the location of the beads in WF are relative to the objective, whereas in TIRF the estimated depth is related to the distance to the glass coverslip. As depicted on Fig. 2*C* and Movie S2, the adjusted model is in good agreement with the measured intensity profiles. Indeed, from these parameter adjustments, the location of the beads can be estimated and the slope of the glass slide recovered (Fig. 2*D*), the latter falling within the confidence interval deducted from the accuracy of the measurement of the different characteristic dimensions of the sample. Finally, from the dispersion of the estimated depth around the average slope (Fig. 2*D*), we can conclude that the localization precision obtained with this approach is higher than the corresponding precision given by estimating the location of the beads in the WF image stack as already mentioned (17).

Estimating the 3D density of fluorophores convolved by the emission point spread function then would simply boil down to inverting the linear system. Some care has to be taken when inverting such system, as the inverse problem is at best badly conditioned. Nevertheless, constraints can be imposed to the solution such as positivity, and, in the case of time-lapse acquisitions, a multiframe regularization can be used in addition to the spatial and temporal regularization smoothness to solve the reconstruction problem. Moreover, to be effective, such a positivity constraint requires a correct knowledge of the background level. As a consequence, for each multiangle image stack, a background image is obtained by driving the beam out of the objective. Given that several convex constraints have to be satisfied at the same time, we propose to rely on a flavor of the PPXA algorithm (26) to estimate the tridimensional density of fluorophores (Fig. S4). More detailed information on how noise, object depth, and the required number of angles can be taken into account is discussed in *SI Imaging Model and Reconstruction* and Fig. S5. Finally, to take into account the variations of the medium index, we select an effective index within a predefined range by minimizing the reconstruction error at each pixel under a spatial smoothness constraint (Fig. S6). It is worth noting that the computation time for the reconstruction on 10 planes from a stack 512 × 512 images corresponding to 21 incidence angles ranges from 1 to 5 min depending on the number of iterations.

Imaging in Vitro and in Vivo Actin Assembly. The proposed multiangle TIRF image reconstruction approach was then tested on complex samples such as actin network architectures for which spatial resolution and dynamics remain an issue. We first challenged the spatial organization of actin nucleation geometry using an in vitro assay based on micropatterning method (27). In this context, the micropatterns promote actin assembly and constrain the actin organization. This system, giving rise to specific architectures (parallel or antiparallel bundles and networks) mimics equivalent structures observed in cells. Three-dimensional reconstruction of multiangle TIRFM stacks clearly highlights the fact that structures assembled outside of the patterned areas extend in depth and are not restricted to the plane of the glass coverslip. This is displayed both in a color-coded depth visualization (Fig. 3*A*), as well as in the thumbnails (Fig. 3*A*, *Right*) corresponding to four equally spaced slices, taken among 10 reconstructed planes. We observe radially expanding bundles located in the first 100-nm range and a second set of filaments located in the 100- to 300-nm range above. The resulting network is not well constrained, generating an unorganized architecture; therefore, bundle crossings appear (Fig. 3*A*). In contrast, the network induced by a circular pattern appears highly organized (Fig. 3*B*). The results obtained with this approach confirm and underscore previously published data (27). Indeed, the gain in axial resolution demonstrates unambiguously that the actin structure arising from the circular pattern is confined next to the patterned coverslip (mainly within the first 50 nm). The analysis presented here emphasizes the structural heterogeneity of actin organization and extent of deformation observed toward the center as a consequence of growing actin bundles encountering each other. This allows the characterization of sites of active force-induced deformation driven by actin assembly.

In a cellular context, depending on the acquisition parameters, an axial resolution of 50–100 nm on average can be reached, over up to 800 nm in depth. This is illustrated in Fig. 3*C* on LifeAct-mCherry–expressing RPE1 cells, where actin architecture can be restored from an image stack corresponding to 21 incidence

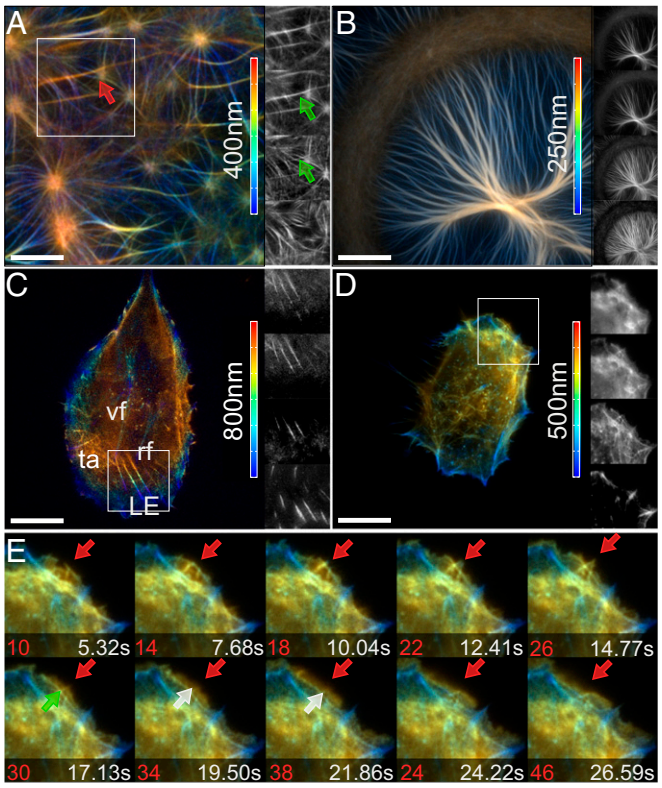

Fig. 3. Three-dimensional actin architecture and dynamics. (*A*) "In vitro" actin assembly on sparsely patterned cover glasses. The structure appears rather unorganized and extending into the *z* direction; note the filament crossings (red arrow on the elevation map, green arrows in the thumbnails on the *Right* corresponding to an area indicated by the white square, showing structures belonging to different planes). (*B*) "In vitro" actin assembly on cover glasses with circular patterns. The structure remains constrained next to the coverslip (50-nm range) and polymerized actin filaments form bundles that encounter at the center of the circle inducing an elevation of this actin structure. (*C*) RPE1 fixed cells expressing LifeAct-mCherry show characteristic actin structures, transverse arcs (ta), radial fibers (rf), ventral stress fibers (vf), as well as the leading edge (LE) of the migrating cell. The elevation map highlights the 3D organization of those structures and thumbnails on the *Right* illustrate the ascendant orientation of the radial fibers. A time-lapse sequence (*D*) and the zoom-in image sequence (*E*) show a protrusion/retraction event (red arrowheads) near the plasma membrane, associated with the formation of a transverse arc in RPE1 cells expressing LifeAct-mCherry.

angles, with a resulting 50-nm axial pixel size after reconstruction of 20 image planes. The color-coded depth visualization reveals that the radial fibers (rf) arising from the leading edge toward the cell center are interconnected by transverse arcs (ta) and indicates location of ventral stress fibers (vf) at the bottom of the cell. Details in actin fibers distribution in depth are also well visualized in planes obtained after reconstruction of a multiangle image stack (Fig. 4*C*, thumbnails). It shows their continuity from the adhesion sites at the leading edge (LE), located on the very first planes (below 50 nm), up to the dorsal cell center (above 650 nm). Six different approaches for reconstructing multiangle TIRF were compared on this image series (*SI Imaging Model and Reconstruction* and Fig. S7).

The fact that high axial resolution can be reached in "streaming overlap" acquisition mode makes our method an approach of choice to study high dynamics of intracellular architectures. This is one asset of the proposed approach as shown in Fig. 3 *D* and *E* on LifeAct-mCherry–expressing RPE1 cells where a 400-nm thickness of actin architecture can be restored from a stack of 10 angles acquired within 590 ms resulting in a 50-nm axial resolution after reconstruction. Different dynamic cell structures such as lamellipodia and filipodia are thus observed with respect to their axial localization, as indicated in the color-coded image or in four planes selected among 10 (thumbnails of the zoomed area in Fig. 3*D*) showing in-depth details at the leading edge of a migrating cell. Time-lapse series of multiangle TIRFM image stacks of moving cells (Fig. 3*E* and Movie S3) were acquired with a frame rate of one stack of 10 angles every 590 ms. Actin shows typical dynamics of extension (protrusion) and retraction where actin-arc addition to the front of the lamella is balanced by actin-arc removal at the back of the lamella. We could visualize in 3D with high axial resolution, features such as actin filaments crossing on top of each other within a growing lamellipodia and transverse arcs conversion to ventral stress fibers anchored to focal adhesions at both ends (28). Consequently, previously unreported aspects of these dynamics are revealed. As visualized at the leading edge of a moving cell, transverse arcs formation connected to adhesion plates appears concomitant to protrusion/retraction events (Fig. 3*E*, red arrowhead). Given the high axial resolution, we could characterize the backward movement of the forming transverse arcs during retraction (Fig. 3*E*, white arrowhead). Movie S4 presents 3D visualizations of another example of actin filament dynamics in a moving cell seen from different angles. In

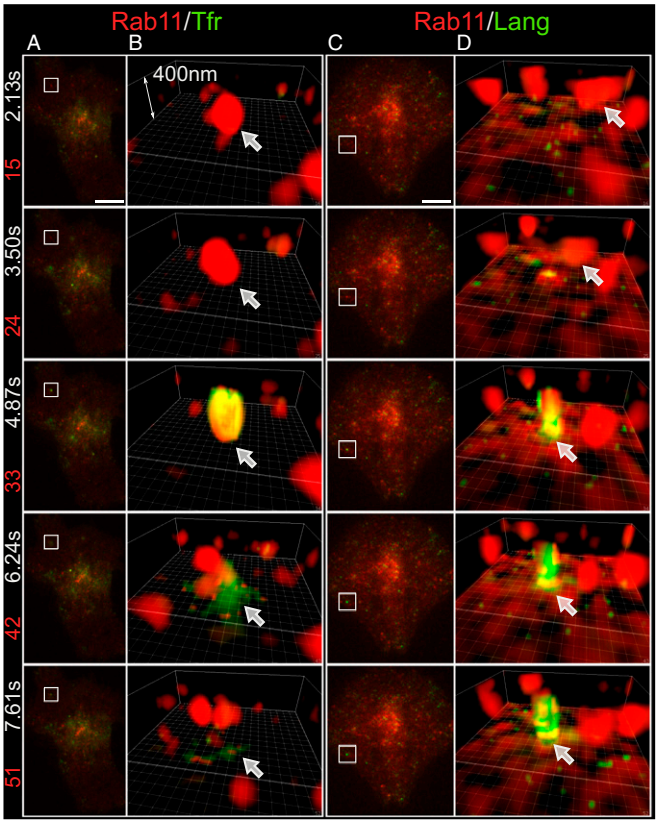

Fig. 4. Three-dimensional reconstruction after multiangle TIRF time-lapse imaging of M10 cells stably expressing TfnR-phluorine/Rab11A-mCherry and eYFP-Langerin/Rab11A-mCherry. Simultaneous dual-color multiangles TIRF stream image stacks constituted of six angles were acquired at 25-ms exposure time per angle for both Rab11/TfnR (left part) and Rab11/Langerin (right part) cells (Movie S5). Only one every nine time points are displayed (on the *Left*, frame numbers appears in red along with the elapsed time in white). Thumbnails (columns *A* and *C*) show entire cells and correspond to images extracted from these stacks for a single incident angle $\theta = 63.53°$. Automatically detected region of interest appear as a cuboid (height, 400 nm; voxel size, 160 × 160 × 40 nm) in the corresponding 3D views (columns *B* and *D*). Elapsed times matching up to the millisecond between the two acquisitions allow a comparative evaluation of the cargo behavior during the docking–fusion process.

this case, time-lapse series of multiangle TIRFM image stacks was acquired at the frame rate of one stack of 11 angles every 5 s with an exposure time of 50 ms per plane. In summary, the high spatial and temporal resolution of our approach is perfectly adapted to the study of actin architectures dynamics during cell migration.

Last Step of Exocytosis and Recycling Processes Imaging. As another biological model, we focused on deciphering the very last steps of exocytosis and recycling processes, using eYFP-Langerin already mentioned in this manuscript as well as TfnR-pHluorin, as reporter molecules. We previously showed that constitutive recycling of the former transmembrane protein strictly depends on a Rab11a platform that coordinates cortical actin anchoring, tethering, and docking of recycling vesicles at the plasma membrane (15). Here, we performed simultaneous double-fluorescence image acquisition using both an eYFP-Langerin/Rab11-mCherry stably expressing cell line and a Rab11-mCherry stably expressing cell line transfected with TfnR-pHluorin. Each of the two sequences described below in details is only one example among hundreds of similar events automatically detected within each single cell (Movie S5). Taking into account the highly dynamic behavior of the recycling vesicles, image series corresponding to simultaneous two colors multiangle TIRF image stacks were recorded at one stack of six angles every 150 ms (at 25-ms exposure time). Three-dimensional reconstructions were performed on the first 400 nm in depth of the cells using a 40-nm axial pixel size. Fig. 4 only sketches few instant snapshots extracted from Movie S5. Selected areas (white squares in Fig. 4 *A* and *C*) in images obtained by a single TIRF angle are compared with a side view of the corresponding cuboid after 3D reconstruction (Fig. 4 *B* and *D*). Taking into account the noticeable continuity in Movie S6, a number of dynamics details that occurs in the *z* axis can be resolved in the 3D reconstructions, such as (*i*) the Rab11a-positive structure movement from inside the cell toward the plasma membrane, (*ii*) the rather heterogeneous delay (up to 10 s) between docking and start of fusion as better illustrated in the red channel in Movie S5 for events detected in both type of cells, (*iii*) the fusion per se as visualized by a bright signal (displayed in green) due to the pH sensitivity of both TfnR-pHluorin (Fig. 4*B*, third row) and eYFP-Langerin (Fig. 4*D*, second and third rows) emission yields, and (*iv*) the concomitant fading of the Rab11a signal from the membrane, which is completed within the next 1.5 ± 0.3 s (SD) in both conditions corresponding to ∼10 frames of the 3D reconstruction (Fig. S8).

Although both types of Rab11a vesicles display a similar exponential decay for Rab11a after fusion, their further behaviors significantly differ. The more or less radial diffusion of TfnR in the very plane of the plasma membrane is almost completed within 2.3 ± 0.1 s (SD) after the beginning of fusion in the majority of automatically detected events (Fig. 4*B*, third vs. fifth row; Fig. S8). In contrast, Langerin signal at the docking site can be stable for long periods of time and keeps a rod shape extending up to 200 nm in the *z* axis, visible in the 3D reconstruction (Fig. 4*D*, third vs. fifth row, and Movie S6).

Accumulation of exocytosis/recycling structures at the plasma membrane during the docking process shows that the movement of vesicles in the cell cannot be merely diffusional. Vesicles must be actively transported toward the membrane, or randomly moving vesicles must become trapped near the membrane. In both cases, vesicles must be held close to the plasma membrane by "tethers," linking it to the membrane or/and to cytoskeletal components before fusion processes occur. This docking delay before actual fusion is rather heterogeneous as illustrated in the red channel in Movie S5 for events detected in both type of cells and can last up to 10 s. Differences in their spatiotemporal behaviors can be directly observed, as illustrated here by the Langerin versus TfnR comportments after vesicle fusion. Finally, the coordinated functions of molecular actors such as Rab11a and its molecular partners involved in these processes are decipherable at the right space and time resolution. In this respect, immediate Rab11a fading after vesicle fusion in the 3D reconstruction is not correlated with a diffusion process in the plane of plasma membrane (Movie S6, upper part), as for TfnR signal.

Discussion

Three-dimensional reconstruction of multiangle TIRFM image stacks is a high-resolution technique dedicated to the temporal definition of biological dynamical events occurring up to 800 nm in depth of the cell. Depending on sampling of the incidence angle, high axial resolution can be reached with high acquisition rate (up to 30 stacks per s). This method gives access to high dynamics of intracellular components. Depending on the signal-to-noise ratio, it allows dense regime acquisition or long-term imaging of live sample with a reduced phototoxicity and bleaching compared with WF or confocal microscopy. Additionally, this imaging approach is compatible with denoising algorithms, allowing even lower light irradiation (29). The 3D reconstruction of multiangle TIRFM image stacks relies on fluorescence intensity, which makes possible quantitative analyses on diffusion or dissociation of molecular components. In this respect, fluorescence recovery or photoactivation approaches are also provided by the described setup and can be combined with our approach on live cells. Finally, this 3D high-resolution TIRF microscopy is direct and undemanding.

The exponentially decreasing intensity of the evanescent wave involved in TIRF microscopy limits the domain of the sample that can be imaged, therefore restricting our approach to the observation of biological events occurring nearby the plasma membrane. Consequently, this method is committed to decipher cellular functions such as diverse morphological effects of cell signaling, membrane remodeling, cortical actin polymerization, and dynamics of endocytosis or exocytosis. Motivated by studies describing a dependency of the tethering/docking/fusion process timing upon the nature of the cargo for identical known actors of the molecular machinery such as Rab11a and other partners (15, 30–32), we compared the latest steps of the Rab11a-dependent TfnR and Langerin recycling pathways. Our approach allows deciphering of this sequence of steps in 3D without temporal compromise. The experimental workflow also includes adaptation of an automated detection algorithm to identify events of interest, the building of a database of these events interactively connected to corresponding image series and finally the 3D+ time reconstruction of multiangle TIRFM of the chosen events (*SI Imaging Model and Reconstruction*). Localization of events allow the characterization of behaviors immediately prior and after fusion, revealing on one hand the progressive nature of tethering and docking in live cells in the 3D space but also making possible the analysis of heterogeneities both within and between experimental conditions (see Movies S5 and S6). Among other information, the delay between the arrest of a Rab11a carrier vesicle at a defined site near the cell surface and the beginning of fusion in the plane of the plasma membrane is measurable (from few hundreds of milliseconds up to second). In contrast, Rab11a vanishes from the recycling vesicles concomitantly to the fusion event and with a similar time constant of the decay phase of 1.01 ± 0.2 s (SD), whatever the studied cargo (TfnR vs. Langerin), in accordance with recent data obtained for the fusion of Rab11/Rhodopsin exocytic vesicles in the apical membrane of MDCK cells (33). Interestingly, the 3D reconstruction provides clues on the mechanism of this Rab11a vanishing, which does not correspond merely to a simple diffusion in the plasma membrane but also reflects a fast dissociation process concomitant to the fusion itself. This enlightens the different decay distributions calculated for Rab11a and TfnR signals after vesicle fusion (Fig. S8), making realistic the hypothesis of Rab11a being recycle from the recycling-exocytic vesicle membranes to the cytosol, immediately once fusion occurs. A molecular platform, minimally constituted of Rab11a, Rab11FIP2, Myosin Vb, and therefore actin, has been recently shown to regulate the dynamics of the latest steps of both TfnR (34) and Langerin recycling (15), whereas only the latter was previously shown to be strictly dependent on Rab11a (35). Several results indicates that

Myosin Vb or Myosin Vb associated with Rab11FIP2 (36) acts at the cell periphery (32), more likely as a braking "tether" for the vesicle onto cortical actin (33). In this respect, the high temporal resolution over the full field of view of our technique should lead to better understanding the space–time coordination between actin fluxes and vesicle tethering–docking, enlightening the relationship between exocytosis and actin dynamics for example within a migrating cell (37).

Finally, a discriminating spatial and temporal behavior of Langerin compared with TfnR after vesicle fusion is revealed in our study. One should mention that, in contrast to TfnR, Langerin organizes itself as multichain complexes and ultimately forms Birbeck granules (BGs) within Langerhans cells or transfected cells and some appear as "open-ended" tubular structures, connected to the plasma membrane by EM studies (23). Whether dissociation kinetics of ternary complexes of Langerin within these latter structures limits further delivery within the plane of the plasma membrane remains to be demonstrated. However, it could lead to the slow diffusion observed in a number of fusion events (Movie S5 and Fig. 4 *C* and *D*). Although infrequently observed at the EM level, such BG-like structures could match up the population of Langerin recycling vesicles (17–21%) showing this phenotype. Moreover, their rod shape is reminiscent of the persistant Langerin structures observed here in the *z* axis (Fig. 4*D*) once fusion started (Movie S6), suggesting that BGs may represent recycling intermediates.

The volume reconstruction approach could be further investigated as taking into account the point spread function of the optical system in the reconstruction algorithm would allow further improvement in the resolution when having a precise knowledge of the focusing point. Finally, although the lateral resolution of the proposed 3D TIRF microscopy approach remains restrained by the Abbe limit, a combination with TIRF structured illumination, if not at the expense of the acquisition rate and the azimuthal averaging property of the setup, could prove an elegant approach to go beyond this barrier and lead to an isotropic high-resolution microscopy technique for live imaging.

Materials and Methods

Biological Material and Sample Preparation. M10 cells stably expressing Langerin tagged with eYFP or expressing both Langerin tagged with eYFP and Rab11a tagged with mCherry, were previously described (14). M10 cells were also transfected with plasmids coding for TfnR-pHluorin, and Rab11a-mCherry, before imaging. RPE1 cells stably expressing LifeAct tagged with mCherry were also used. To normalize experimental data in some experiments when indicated, cells were platted onto fibronectin Cytoo chips (Cytoo Cell Architect). The micropatterning method for actin polymerization was described in ref. 26.

Microscopy. Our setup is based on an inverted microscope equipped with the proposed spinning TIRF module, providing dual color microscopy. This system is interfaced with hardware and software implementations allowing the full control of the illumination incident angle as a function of penetration depth, theoretical refractive indexes, and laser wavelengths. Images are acquired using either an Evolve 512 or Evolve 512 delta (Photometrics) EMCCD camera.

Full and detailed materials and methods are available in *SI Materials and Methods* including acquisition software, image processing, and reconstruction methods.

ACKNOWLEDGMENTS. We thank Drs. C. Kervrann and J. Sedat for fruitful discussions. The Plateforme Imagerie Cellulaire et Tissulaire–Infrastructure en Biologie Santé et Agronomie Imaging Facility of the Institut Curie is member of the "France-BioImaging" national research infrastructure (ANR-10-INBS-04). Part of data presented in Fig. 3 were obtained during the CNRS summer school "MiFoBIO 2012." Funding was provided by the Fondation de la Recherche Médicale (Contract 20111123020). For this study, C. Guérin, F.S., and L.B. are financed by the Labex Grenoble Alliance for Integrated Structural Cell Biology.

1. Hell SW, Wichmann J (1994) Breaking the diffraction resolution limit by stimulated emission: Stimulated-emission-depletion fluorescence microscopy. *Opt Lett* 19(11):780–782.
2. Rust MJ, Bates M, Zhuang X (2006) Sub-diffraction-limit imaging by stochastic optical reconstruction microscopy (STORM). *Nat Methods* 3(10):793–796.
3. Hess ST, Girirajan TP, Mason MD (2006) Ultra-high resolution imaging by fluorescence photoactivation localization microscopy. *Biophys J* 91(11):4258–4272.
4. Betzig E, et al. (2006) Imaging intracellular fluorescent proteins at nanometer resolution. *Science* 313(5793):1642–1645.
5. Heilemann M, et al. (2008) Subdiffraction-resolution fluorescence imaging with conventional fluorescent probes. *Angew Chem Int Ed Engl* 47(33):6172–6176.
6. Subach FV, Patterson GH, Renz M, Lippincott-Schwartz J, Verkhusha VV (2010) Bright monomeric photoactivatable red fluorescent protein for two-color super-resolution sptPALM of live cells. *J Am Chem Soc* 132(18):6481–6491.
7. Galbraith CG, Galbraith JA (2011) Super-resolution microscopy at a glance. *J Cell Sci* 124(Pt 10):1607–1611.
8. Gustafsson MG (2000) Surpassing the lateral resolution limit by a factor of two using structured illumination microscopy. *J Microsc* 198(Pt 2):82–87.
9. Orieux F, Sepulveda E, Loriette V, Dubertret B, Olivo-Marin JC (2012) Bayesian estimation for optimized structured illumination microscopy. *IEEE Trans Image Process* 21(2):601–614.
10. Axelrod D, Burghardt TP, Thompson NL (1984) Total internal reflection fluorescence. *Annu Rev Biophys Bioeng* 13:247–268.
11. Pawley JB, ed (1995) *Handbook of Biological Confocal Microscopy* (Springer, New York).
12. Denk W, Strickler JH, Webb WW (1990) Two-photon laser scanning fluorescence microscopy. *Science* 248(4951):73–76.
13. Allersma MW, Wang L, Axelrod D, Holz RW (2004) Visualization of regulated exocytosis with a granule-membrane probe using total internal reflection microscopy. *Mol Biol Cell* 15(10):4658–4668.
14. Burchfield JG, Lopez JA, Mele K, Vallotton P, Hughes WE (2010) Exocytotic vesicle behaviour assessed by total internal reflection fluorescence microscopy. *Traffic* 11(4):429–439.
15. Gidon A, et al. (2012) A Rab11A/myosin Vb/Rab11-FIP2 complex frames two late recycling steps of langerin from the ERC to the plasma membrane. *Traffic* 13(6):815–833.
16. Mattheyses AL, Shaw K, Axelrod D (2006) Effective elimination of laser interference fringing in fluorescence microscopy by spinning azimuthal incidence angle. *Microsc Res Tech* 69(8):642–647.
17. Fiolka R, Belyaev Y, Ewers H, Stemmer A (2008) Even illumination in total internal reflection fluorescence microscopy using laser light. *Microsc Res Tech* 71(1):45–50.
18. van't Hoff M, de Sars V, Oheim M (2008) A programmable light engine for quantitative single molecule TIRF and HILO imaging. *Opt Express* 16(22):18495–18504.
19. Axelrod D (1981) Cell-substrate contacts illuminated by total internal reflection fluorescence. *J Cell Biol* 89(1):141–145.
20. Olveczky BP, Periasamy N, Verkman AS (1997) Mapping fluorophore distributions in three dimensions by quantitative multiple angle-total internal reflection fluorescence microscopy. *Biophys J* 73(5):2836–2847.
21. Rohrbach A (2000) Observing secretory granules with a multiangle evanescent wave microscope. *Biophys J* 75(5):2641–2654.
22. Yang Q, Karpikov A, Toomre D, Duncan JS (2011) 3-D reconstruction of microtubules from multi-angle total internal reflection fluorescence microscopy using Bayesian framework. *IEEE Trans Image Process* 20(8):2248–2259.
23. McDermott R, et al. (2004) Reproduction of Langerin/CD207 traffic and Birbeck granule formation in a human cell line model. *J Invest Dermatol* 123(1):72–77.
24. Gingell D, Heavens OS, Mellor JS (1987) General electromagnetic theory of total internal reflection fluorescence: The quantitative basis for mapping cell-substratum topography. *J Cell Sci* 87(Pt 5):677–693.
25. Reichert WM, Truskey GA (1990) Total internal reflection fluorescence (TIRF) microscopy. I. Modelling cell contact region fluorescence. *J Cell Sci* 96(Pt 2):219–230.
26. Combettes P, Pesquet J-C (2011) Proximal splitting methods in signal processing. In *Fixed-Point Algorithms for Inverse Problems in Science and Engineering*, eds Bauschke HH, et al. (Springer, New York), pp 185–212.
27. Reymann AC, et al. (2010) Nucleation geometry governs ordered actin networks structures. *Nat Mater* 9(10):827–832.
28. Hotulainen P, Lappalainen P (2006) Stress fibers are generated by two distinct actin assembly mechanisms in motile cells. *J Cell Biol* 173(3):383–394.
29. Carlton PM, et al. (2010) Fast live simultaneous multiwavelength four-dimensional optical microscopy. *Proc Natl Acad Sci USA* 107(37):16016–16022.
30. Fan GH, Lapierre LA, Goldenring JR, Sai J, Richmond A (2004) Rab11-family interacting protein 2 and myosin Vb are required for CXCR2 recycling and receptor-mediated chemotaxis. *Mol Biol Cell* 15(5):2456–2469.
31. Parent A, Hamelin E, Germain P, Parent JL (2009) Rab11 regulates the recycling of the beta2-adrenergic receptor through a direct interaction. *Biochem J* 418(1):163–172.
32. Baetz NW, Goldenring JR (2013) Rab11-family interacting proteins define spatially and temporally distinct regions within the dynamic Rab11a-dependent recycling system. *Mol Biol Cell* 24(5):643–658.
33. Thuenauer R, et al. (2014) Four-dimensional live imaging of apical biosynthetic trafficking reveals a post-Golgi sorting role of apical endosomal intermediates. *Proc Natl Acad Sci USA* 111(11):4127–4132.
34. Schafer JC, et al. (2014) Rab11-FIP2 interaction with MYO5B regulates movement of Rab11a-containing recycling vesicles. *Traffic* 15(3):292–308.
35. Uzan-Gafsou S, et al. (2007) Rab11A controls the biogenesis of Birbeck granules by regulating Langerin recycling and stability. *Mol Biol Cell* 18(8):3169–3179.
36. Hales CM, et al. (2001) Identification and characterization of a family of Rab11-interacting proteins. *J Biol Chem* 276(42):39067–39075.
37. Burnette DT, et al. (2011) A role for actin arcs in the leading-edge advance of migrating cells. *Nat Cell Biol* 13(4):371–381.